This is an open access article published under a Creative Commons Attribution (CC-BY) License, which permits unrestricted use, distribution and reproduction in any medium, provided the author and source are cited.

ACS AUTHORCHOICE

CHEMISTRY OF MATERIALS

pubs.acs.org/cm

Article

Rapid Low-Dimensional Li^+ Ion Hopping Processes in Synthetic Hectorite-Type $Li_{0.5}[Mg_{2.5}Li_{0.5}]Si_4O_{10}F_2$

Caroline Hiebl,[#] Patrick Loch, Marina Brinek,[#] Maria Gombotz, Bernhard Gadermaier, Paul Heitjans,* Josef Breu, and H. Martin. R. Wilkening*

Cite This: *Chem. Mater.* 2020, 32, 7445−7457

Read Online

ACCESS | Metrics & More | Article Recommendations | Supporting Information

ABSTRACT: Understanding the origins of fast ion transport in solids is important to develop new ionic conductors for batteries and sensors. Nature offers a rich assortment of rather inspiring structures to elucidate these origins. In particular, layer-structured materials are prone to show facile Li^+ transport along their inner surfaces. Here, synthetic hectorite-type $Li_{0.5}[Mg_{2.5}Li_{0.5}]Si_4O_{10}F_2$, being a phyllosilicate, served as a model substance to investigate Li^+ translational ion dynamics by both broadband conductivity spectroscopy and diffusion-induced ^7Li nuclear magnetic resonance (NMR) spin−lattice relaxation experiments. It turned out that conductivity spectroscopy, electric modulus data, and NMR are indeed able to detect a rapid 2D Li^+ exchange process governed by an activation energy as low as 0.35 eV. At room temperature, the bulk conductivity turned out to be in the order of 0.1 mS cm^{-1}. Thus, the silicate represents a promising starting point for further improvements by crystal chemical engineering. To the best of our knowledge, such a high Li^+ ionic conductivity has not been observed for any silicate yet.

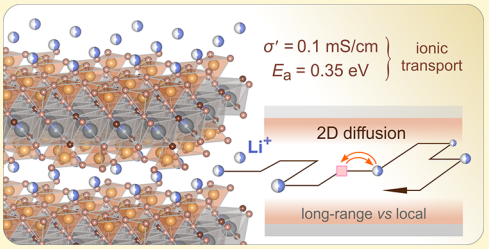

Downloaded via 89.245.22.243 on February 26, 2024 at 08:26:27 (UTC).
See https://pubs.acs.org/sharingguidelines for options on how to legitimately share published articles.

1. INTRODUCTION

The diffusion of small cations and anions plays an important role in many devices such as sensors[1−3] and batteries.[4−11] Although for some applications, e.g., in the semiconductor industry[12] or in the development of breeding materials[13−15] for fusion reactor blankets, diffusion is unwanted, in other branches, materials with extremely high diffusion coefficients are desired.[16−21] Finding the right material and tailoring its dynamic properties further requires an in-depth understanding of the origins that determine fast ion dynamics.[22−26]

In many cases, layer-structured materials[27−30] are known to offer fast diffusion pathways along the buried interfaces or between larger gaps inside the crystal structure.[31] Commonly, powder samples are synthesized and investigated; however, polycrystalline samples do not allow orientation-dependent measurements of ionic conductivity. Fortunately, anisotropic properties of ionic transport in polycrystalline samples can be probed by nuclear magnetic resonance (NMR) spin−lattice relaxation experiments.[5,30,32−35] The most prominent examples, whose Li^+ diffusion properties were studied in this way,[36] include graphite[37,38] or transition metal chalcogenides such as TiS_2,[39−43] NbS_2,[44,45] and SnS_2.[46] Recently, two-dimensional (2D) Li^+ diffusion has also been determined in hexagonal $LiBH_4$.[29,47] Fast fluoride, F^-, diffusion is observed in $MeSnF_4$ (Me = Pb, Ba) and, as has been shown quite recently, also in layer-structured $RbSn_2F_5$.[48] In these materials, spatial constraints guide the ions over long distances. The principle of guided ions has also been found in $Li_{12}Si_7$.[49,50] In binary silicide, the Li^+ ions are subjected to a fast one-dimensional diffusion process along the surface of a virtual pipe formed by the stacked Si_5 rings.[49] In channel-structured materials with the ions diffusing *inside* the channels, their diffusion pathways may, however, easily be blocked by foreign, immobile ions.[51] The same effect might, of course, also influence 2D translational ion dynamics but to a lesser degree.

To understand Li^+ diffusion in structures offering 2D diffusion pathways, we chose hectorite-type $Li_{0.5}[Mg_{2.5}Li_{0.5}]Si_4O_{10}F_2$ as a model system, see Figure 1, and studied the Li^+ self-diffusion properties and electrical ionic transport. While the latter is investigated by broadband conductivity spectroscopy,[52] we took advantage of ^7Li NMR spin−lattice relaxation measurements[32,53] to shed light on Li^+ translational dynamics.

Hectorite is, as montmorillonite, a clay mineral of the smectite group (gr. *σμηκτις*, soil with the ability to clean, to soak something up, e.g., swelling through water uptake). Such silicates belong to the family of phyllosilicates (gr. *φυλλο*, leaf). Fluorohectorite is a 2D host material with a rigid 2:1 sandwich-like structure;[54] each lamella is composed of two silicate and one Mg^{2+} rich layer where the earth alkaline cations are octahedrally coordinated by oxygen and fluorine anions. An idealized structure of synthetic (turbostratic) Li-bearing

Received: June 12, 2020
Revised: August 5, 2020
Published: August 5, 2020

ACS Publications

© 2020 American Chemical Society

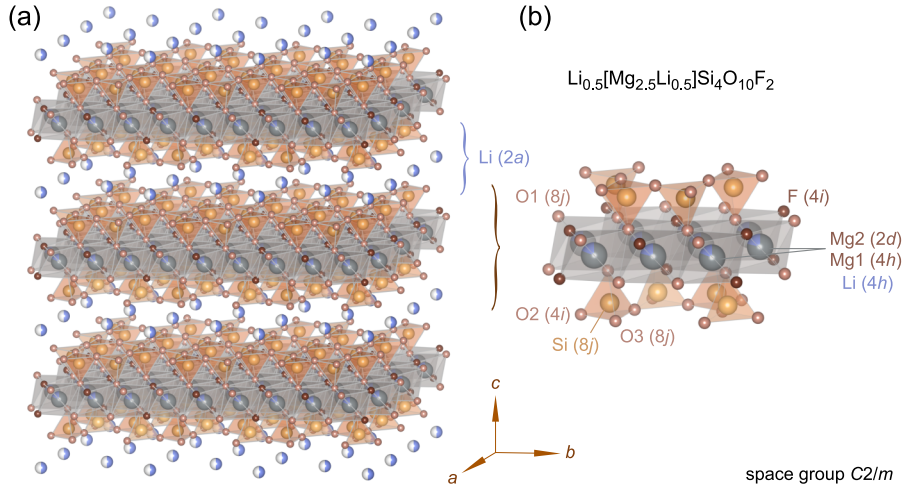

Figure 1. (a) Idealized crystal structure of hectorite-type $Li_{0.5}[Mg_{2.5}Li_{0.5}]Si_4O_{10}F_2$ (drawn according to the space group *C*2/*m*, the real structure is clearly turbostratic) with two distinct crystallographic sites occupied by the Li ions. Those between the Mg-rich layers (see (b)), which are here shown following a homogenous charge distribution, are expected to have access to fast 2D diffusion pathways.

fluorohectorite $[Li_{0.5}]^{inter}[Mg_{2.5}Li_{0.5}]^{octa}[Si_4]^{tetra}O_{10}F_2$ is shown in Figure 1. Natural hectorite of the composition $Na_{0.3}(Mg, Li)_3Si_4O_{10}(OH)_2$, including also minor amounts of Ca^{2+}, K^+, and Al^{3+}, was named for its occurrence 5 km south of Hector (San Bernardino County, California, USA).[55] It was first described in 1941 and found in a bentonite deposit, altered from clinoptilolite, a natural zeolite, derived from volcanic tuff and ash with a high glass content.[55] Cation exchange strategies allow one to effectively replace the Na ions in hectorite by Li ions; also larger inorganic or organic molecules (pillars) can be introduced, resulting in porous so-called pillared clays.[54] Exemplarily, the Khan group successfully used hectorite-based materials as passive and active filler materials to prepare nanocomposite polymer-based (gel) electrolytes as well as to develop composite $LiCoO_2$-based cathode materials.[56−59] Here, our hypothesis is that the interlayer gap in such host structures, particularly that of hectorite, offers indeed fast diffusion pathways for small charge carriers such as Li^+ and Na^+ ions.

Verifying the hypothesis of 2D transport is, however, challenging if only powder samples are available at hand. Fortunately, ^{7}Li NMR spin−lattice relaxation measurements,[49,53] also successfully used to characterize electrolytes for batteries,[60,61] represent a unique tool to study such anisotropic properties even for powdered samples, since the spectral density functions J governing the NMR spin−lattice relaxation rates $1/T_1$ ($\propto J$) possess specific features for 1, 2, and 3D ion transport.[30,62] As intimated above, low-dimensional ionic transport has, so far, been probed only for a limited number of materials by NMR relaxation techniques.[36] The present study contributes to this research field and is aimed at answering the question whether 2D silicate structures offer an assortment of materials with enhanced ion diffusion properties.

2. EXPERIMENTAL SECTION

2.1. Preparation and Characterization of $Li_{0.5}[Mg_{2.5}Li_{0.5}]Si_4O_{10}F_2$. Lithium fluorohectorite with the nominal composition of $Li_{0.5}[Mg_{2.5}Li_{0.5}]<Si_4>O_{10}F_2$ was prepared by a two-step ion exchange procedure starting from melt synthesized Na-fluorohectorite ($Na_{0.5}[Mg_{2.5}Li_{0.5}]<Si_4>O_{10}F_2$). The Na-fluorohectorite was synthesized according to a preparation route published earlier.[54,63] To ensure the complete exchange of Na^+ by Li^+, Na-fluorohectorite was first treated with *n*-butylammonium chloride ($C_4H_{12}ClN$ (C4), 2 M) using a 100-fold excess of its cation exchange capacity (CEC) to obtain the so-called C4-fluorohectorite. Typically, 500 mg of Na-fluorohectorite was exchanged overnight five times with 40 mL of C4 solution at 80 °C. The resulting product was washed five times with an ethanol−water mixture (1:1) and once more with pure ethanol. Atomic absorption spectroscopy (AAS), see below, was used to check the completeness of the ion exchange reaction. After this, the dried C4-fluorohectorite was treated with a 100-fold excess of the CEC of LiOH (2 M, 4 times 40 mL, 6 h, room temperature). While removing excessive LiOH by washing 6 times with 40 mL of deionized water, the ionic strength decreased to a value lower than 0.02 M; furthermore, complete delamination by repulsive osmotic swelling was observed.[63−66] Finally, the gel of delaminated Li-fluorohectorite was freeze-dried followed by vacuum drying at 160 °C.

2.1.1. AAS. To verify complete Na^+-exchange, AAS was used. For this purpose, approximately 20 mg of the samples were weighed into clean Teflon-flasks of 15 mL volume. After the addition of 1.5 mL of 30 wt % HCl (Merck), 0.5 mL of 85 wt % H_3PO_4 (Merck), 0.5 mL of 65% HNO_3 (Merck), and 1 mL of 48 %HBF_4 (Merck), the samples were digested in a 1200 Mega microwave digestion apparatus (MLS, Mikrowellen-Labor-Systeme) for 6.5 min and heated at 600 W. Afterward, the closed sample container was cooled to room temperature; the clear solution was diluted to 100 mL in a volumetric flask and analyzed with a Varian AA100-spectrometer. To determine the Na^+-content by AAS, a five-point calibration curve (0.0 to 0.2 mg/100 mL) was measured by diluting a Na^+ standard AAS-solution (1000 mg/mL) in nitric acid.

2.1.2. CHN-Analysis. A Elementar Unicode equipped with a combustion tube filled with tungsten(VI)-oxide-granules was used to analyze the elements C, H, and N at a combustion temperature of 1050 °C. Samples were dried at 120 °C prior to the measurement.

2.1.3. Physisorption Measurements. Argon adsorption measurements were performed using a Quantachrome Autosorb at 87.35 K using samples that were dried at 120 °C for 24 h in a high vacuum. The pore sizes and volumes were calculated using a nonlocal DFT model (software version 2.11, Ar on zeolite/silica, cylindrical pores, equilibrium model).

2.2. Conductivity Spectroscopy. To perform broadband conductivity measurements, the hectorite sample was first ground in a mortar before the sample was uniaxially pressed (0.5 tons) into a cylindrical pellet with a diameter of 5 mm and a thickness of approximately 1 mm; the exact thickness was determined with a vernier calliper. The pellet was equipped on both sides with Au electrodes that blocked Li^+ ion transport. For this purpose, we used an EM SCD 050 sputter coater from LEICA. The thickness (100 nm) was controlled with a quartz thickness monitoring system. The pellet was then placed inside an active ZGS cell (Novocontrol), which was

https://dx.doi.org/10.1021/acs.chemmater.0c02460
Chem. Mater. 2020, 32, 7445−7457

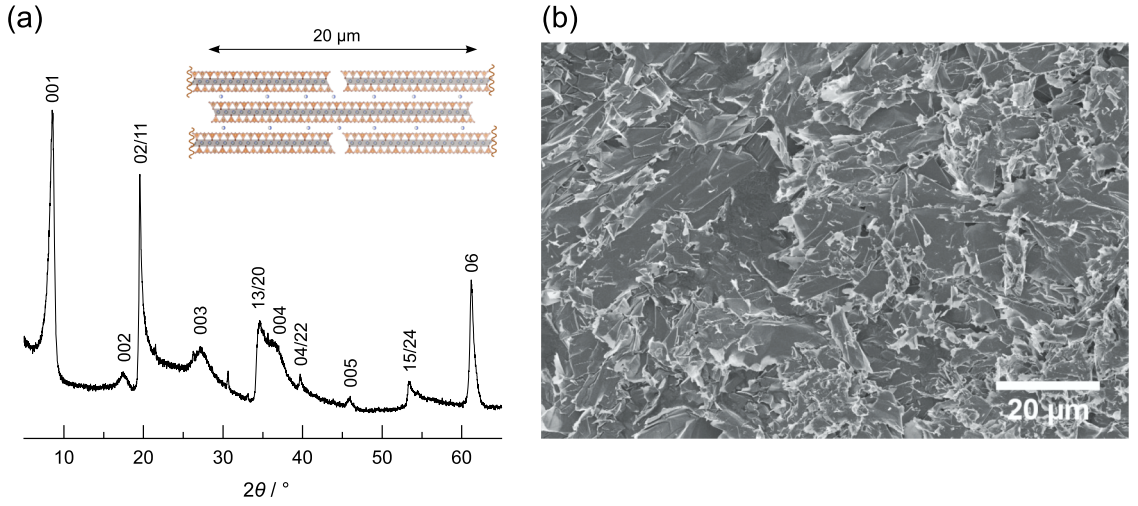

Figure 2. (a) Powder X-ray diffraction pattern of dry Li-fluorohectorite $Li_{0.5}[Mg_{2.5}Li_{0.5}]Si_4O_{10}F_2$ with marked reflections of the 00 L series and the *hk* bands; the inset shows the representative bandlike structure of the hectorite. (b) Scanning electron micrograph of freeze-dried and partially restacked Li-fluorohectorite.

connected to a Novocontrol Concept 80 broadband dielectric spectrometer. We measured the complex impedance, conductivity, and permittivity as a function of temperature and in a frequency range of 0.01 Hz to 10 MHz. The ZGS sample holder was placed in a cryostat, allowing us to measure conductivity isotherms from 133 to 433 K in steps of 20 K. Temperature regulation and monitoring was carried out with a QUATRO controller (Novocontrol). In order to eliminate residual moisture, the pellet was pre-dried in the impedance cell at 433 K (160 °C) for 4 h. During the entire measurement, the impedance cell was permanently flushed with dry, freshly evaporated nitrogen gas.

2.3. Magic Angle Spinning (MAS) NMR. ^{6}Li (73.6 MHz, 120 W power amplifier, 1024 scans, recycle delay $5T_1$ (see below), pulse length 3 μs) and ^{19}F (470.6 MHz, 50 W, 32 scans, recycle delay 1 s, pulse length 2.1 μs) MAS one-pulse NMR spectra were recorded with a 500-MHz Avance spectrometer (Bruker). The measurements were carried out at a rotation speed of 25 kHz using 2.5 mm rotors. The spectra were recorded using one-pulse sequences with ambient bearing gas. Crystalline $LiCH_3COO$ and liquid $CFCl_3$ served as reference materials to determine the isotropic chemical shifts δ_{iso}.

2.4. Time-Domain ^{7}Li NMR Measurements. To prepare the sample for NMR measurements, the hectorite powder sample was ground using a mortar and pestle under an Ar atmosphere in a glove box. After this, it was dried in a vacuum at 160 °C before being fire-sealed in Duran ampoules under vacuum. We recorded both ^{7}Li NMR spectra and ^{7}Li NMR spin−lattice relaxation rates as a function of temperature (173 to 433 K). For this purpose, we used a Bruker 300-MHz spectrometer that was connected to a Bruker cryomagnet with a nominal magnetic field of 7 T. This field corresponds to a nominal ^{7}Li Larmor frequency of $\omega_0/2\pi$ = 116 MHz. While laboratory frame spin−lattice relaxation rates ($1/T_1$) were recorded with the saturation recovery pulse sequence,[67] the spin-lock technique[67,68] was applied to measure transversal magnetization transients leading to the rate $1/T_{1\rho}$, which characterizes spin−lattice relaxation in the so-called rotating frame of reference. The 90° pulse length (t_p) was 2 μs (200 W broadband amplifier) and showed only a slight dependence on temperature. To measure $1/T_1$, we used a comb of 10 closely spaced (80 μs) radio frequency pulses to destroy any longitudinal magnetization M. The subsequent recovery of M as a function of the delay time t_d (4 scans) was followed with a 90° detection pulse; the delay between each scan, although not needed, was set to 1 s. In general, $M(t_d)$ follows a stretched exponential behavior according to $M(t_d) = M_0(1 - \exp[-(t_d/T_1)^{\gamma'}])$, $0<\gamma'\leq 1$. M_0 denotes the equilibrium magnetization that is reached at $t_d \rightarrow \infty$. Here, $M(t_d)$ follows a bi-exponential behavior if the full area under the free induction decays (FIDs) is used to construct $M(t_d)$, see the Supporting Information, Figure S2. In this case, we used a sum of stretched exponentials to parameterize the transient.[31,69,70] Alternatively, the two components of the FIDs were separately analyzed, as explained below. For the corresponding spin-lock $M_\rho(t_d)$ transients (see also Figure S2), we used a single, stretched exponential function to analyze the decay functions: $M_\rho(t_{lock}) \propto \exp[-(t_{lock}/T_{1\rho})^{\gamma}])$, t_{lock} denotes the duration of the locking pulse. We varied t_{lock} from 30 μs to 30 ms (8 scans per locking time) and used a power level that results in a locking frequency $\omega_1/2\pi$ of ca. 20 kHz. The recycle delay between each scan was at least $5T_1$. This value is orders of magnitude lower than $\omega_0/2\pi$ used for the laboratory-frame measurements; hence, spin-lock NMR is sensitive to much slower Li ion dynamics compared to probing via T_1 measurements.

3. RESULTS AND DISCUSSION

3.1. Synthesis of the Li-Fluorohectorites. Direct melt synthesis of Li-fluorohectorites is troublesome. In general, melt-synthesized Li-fluorohectorites may contain a range of impurities and could suffer from isomorphous substitution effects. Thus, the charge density of the silicate layers turned out to be heterogeneous as described earlier.[71] In contrast to the Li-bearing compound, melt synthesis of Na-fluorohectorite followed by long-term annealing yields phase pure materials with a homogenous charge density and, thus, a uniform intracrystalline reactivity.[54,63] This uniform intracrystalline reactivity is especially important for a uniform cation distribution in the interlayer space, which in turn is expected to have a considerably high impact on cation transport properties. Therefore, the Li-fluorohectorite used for the present study was prepared by taking advantage of a complete ion exchange of Na-fluorohectorite. Unfortunately, the affinity of Li^+ for the interlayer space of hectorites is lower than that of Na^+.[72] Consequently, complete ion exchange could not be accomplished directly, even at very high incoming Li^+-concentrations. Therefore, Na^+ was fully exchanged with C4 taking advantage of the much higher selectivity of organic cations for the interlayer space.[73] The completeness of ion exchange at this stage was verified by AAS.

In the next step, Li exchange to Li-fluorohectorite could be driven by deprotonation of the intercalated C4. Elemental analysis proved complete replacement of C4 within experimental errors. At low ionic strength, i.e., at values being smaller than 0.02 M as achieved during the washing

https://dx.doi.org/10.1021/acs.chemmater.0c02460
Chem. Mater. 2020, 32, 7445−7457

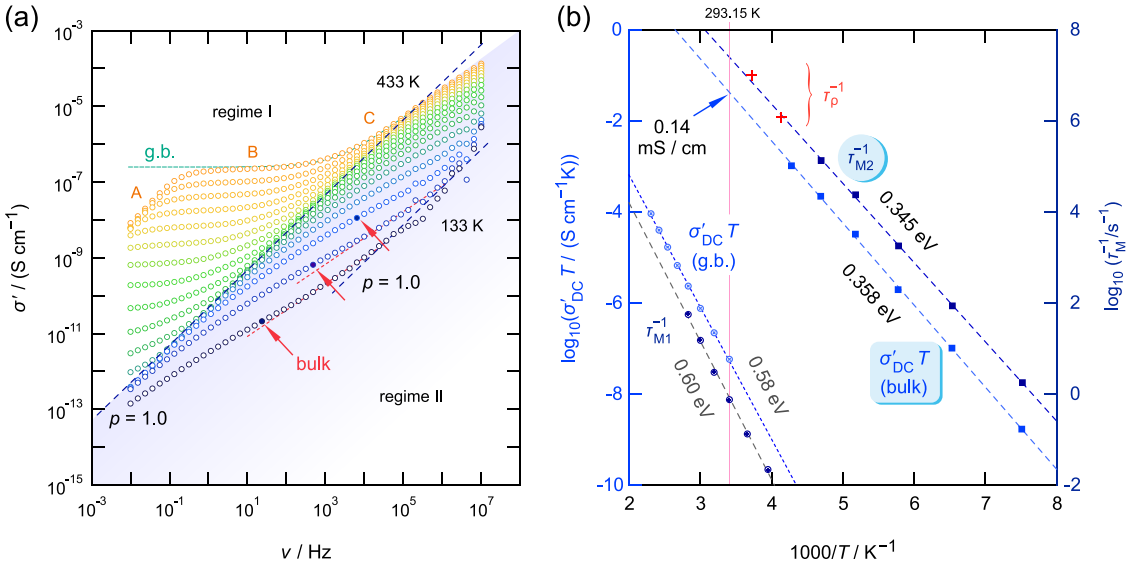

Figure 3. (a) Conductivity isotherms of layer-structured, hectorite-type $Li_{0.5}[Mg_{2.5}Li_{0.5}]Si_4O_{10}F_2$ recorded from T = 133 K to T = 433 K; the measurements span a frequency range of 9 decades. In regime I, the isotherms are governed by the grain boundary (g.b.) response, while in regime II, bulk properties dominate the shape of the curves. See text for further details. (b) Arrhenius plot showing both $\log_{10}(\sigma'_{DC}T/(S\ cm^{-1}\ K))$ and $\log_{10}(1/\tau_M\ /\ s^{-1})$ vs. the inverse temperature $1000/T$. The left axis refers to σ'_{DC} showing either the temperature behavior of the bulk ion conductivity or that governed by the highly resistive g.b. regions. The latter denotes the total conductivity seen in regime I of the isotherms shown in (a). $1/\tau_{Mi}$ refers to the two maxima (i = 1, 2) seen in the electric modulus curves $M''(\nu)$, see Figure 4b, whereas $1/\tau_{M1}$ refers to the g. b. response and $1/\tau_{M1}$ denotes the characteristic electrical relaxation rates of the $M''(\nu)$-peak representing the bulk response. Lines, either dashed or dotted, show Arrhenius fits with the activation energies indicated. At room temperature, $\sigma'_{DC,\ bulk} \approx 0.14$ mS cm^{-1} is expected through extrapolation of the Arrhenius line shown. For comparison, the rates $1/\tau_\rho$ from electrical resistivity measurements carried out at a fixed frequency (1.2 MHz, 10 MHz, see Figure 5b) are included as well.

procedure,[63] Li-hectorite delaminates spontaneously in aqueous suspension by repulsive osmotic swelling whereupon a liquid crystalline gel is obtained. Freeze drying of this gel leads to a voluminous, spongelike, and hierarchically porous material (Figure 2b).

The powder X-ray diffraction pattern of dry Li-fluorohectorite is shown in Figure 2a and shows the characteristic reflections of the *00 L*-series with a basal spacing of 10.2 Å. Missing *hkl* reflections and occurrence of the *λ*-shape of *02/11-*, *13/20-*, *04/22-*, *15/24-*, and *06*-bands indicated a turbostratic type of stacking of adjacent silicate layers. Upon drying, partial restacking is forced with large overlapping areas between adjacent individual layers (20 μm diameter) and leads to bandlike aggregate structures (Figure 1b). Consequently, Li^+ cations are residing at external basal planes and in the interlayer space. The ratio of the two Li sites can only be estimated. The thickness of the restacked tactoids cannot be determined by analyzing the full width at half maximum (fwhm) of basal reflections via the Scherrer equation because the broadening is largely determined by random interstratification of the slightly varying stacking vector. Because of turbostratic disorder, the PXRD pattern contains little structural information beyond basal spacing, which is obvious when comparing a simulated XRD pattern (see Figure S1) for a hypothetical, fully 3D ordered Li-hectorite structure (*C*2/*m* (no. 12), a = 5.25(2) Å, b = 9.08(3) Å, c = 10.37(4) Å, β = 96.51(8)°). Since the *hk*-bands are located approximately at the position of *hk0* reflections, this unit cell could be refined by applying the experimental turbostratic pattern, although with some uncertainty in the *ab*-dimensions. As ion exchange is a topotactic reaction, the structure of the silicate layers is fully preserved as indicated by *ab*-dimensions being similar to dimensions found for a 3D ordered member of the hectorite family (a = 5.2434(10) Å; b = 9.0891(18) Å).[74] The latter, refined structure of the silicate layer could, therefore, be safely applied to obtain Figure 1 and to draw the scheme shown in the inset of Figure 2a.

As the interlayer surface area in the collapsed dry state is not accessible to probe gas molecules, the degree of restacking can, however, be deduced from the specific surface area determined by physisorption. Given the large diameter, the contribution of edges to the total surface area can be safely neglected. The specific surface area per gram for an individual delaminated silicate layer was calculated from the known *ab* dimension and the formula weight. The ratio of this calculated surface area (759.368 m^2/g) and the surface area measured by Brunauer–Emmett–Teller analysis (5.174 m^2/g) yields the average number n_l of layers in the stack, n_l = 147. This estimation indicates that most of the Li^+ ions are indeed located in the interlayer space.

3.2. Ionic Transport and Li^+ Diffusivity. In Figure 3a, the broadband conductivity isotherms of layer-structured $Li_{0.5}[Mg_{2.5}Li_{0.5}]Si_4O_{10}F_2$ are shown. The isotherms, which show the real part of the complex conductivity σ' as a function of frequency ν, were recorded over a dynamic range of 9 decades.

The conductivity curves can be subdivided into several parts, labelled A, B, and C (Figure 3a). To explain these features, we first consider the isotherm recorded at the highest temperature, that is, at T = 433 K (regime I). At low frequencies ν, electrode polarization appears, which manifests itself as a drop in conductivity (A). With increasing frequency, σ' enters the so-called direct current (DC) plateau that corresponds to long-range ion transport in $Li_{0.5}[Mg_{2.5}Li_{0.5}]Si_4O_{10}F_2$ (B). The associated capacitance C of this distinct plateau is in the order of 300 pF (= C_{gb}). Without any doubt, such a high value

https://dx.doi.org/10.1021/acs.chemmater.0c02460
Chem. Mater. 2020, 32, 7445−7457

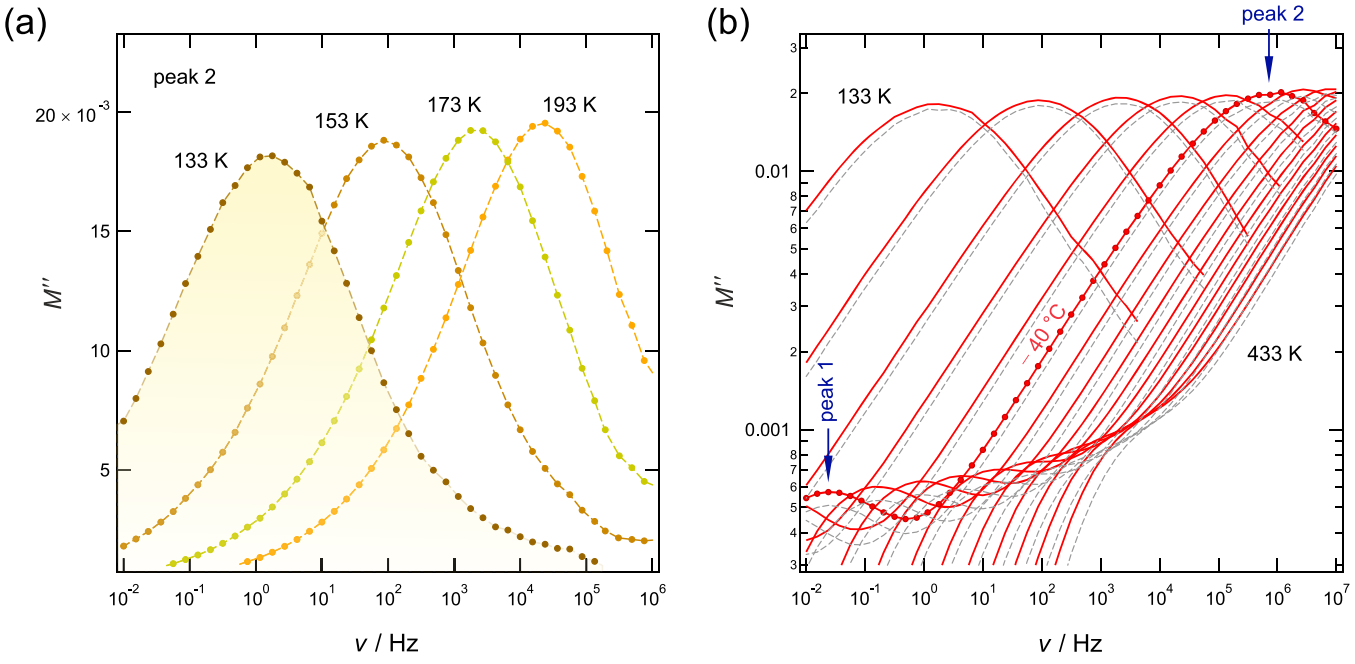

Figure 4. (a) Electrical modulus curves $M''(\nu)$ of hectorite-type $Li_{0.5}[Mg_{2.5}Li_{0.5}]Si_4O_{10}F_2$, which were recorded at the temperatures indicated. (b) Same curves as in (a) but using a double logarithmic plot to visualize also those peaks that are governed by a higher permittivity (and capacitance), see arrow pointing at the peak that appears at 0.03 Hz (233 K). The latter reflects g.b. responses, while the main modulus peaks are produced by bulk electrical relaxation processes characterized by a much lower permittivity, see the arrow pointing at the peak at $\nu = 8 \times 10^5$ Hz. The dashed lines show the response of a measurement on a second pellet prepared, indicating the good reproducibility of the analysis.

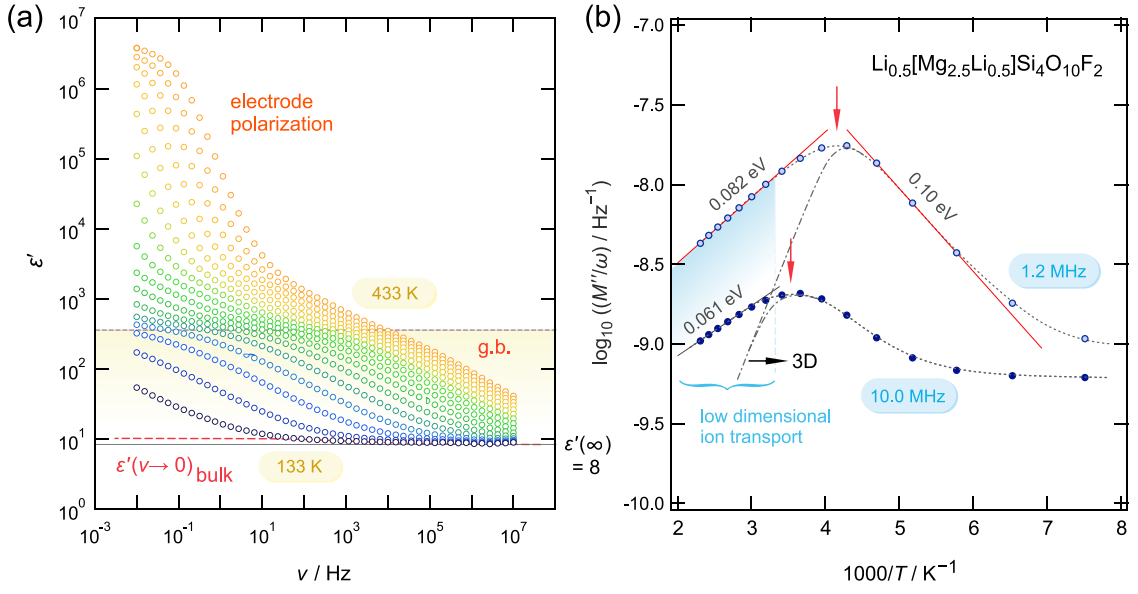

Figure 5. (a) Change of the electrical permittivity of layer-structured $Li_{0.5}[Mg_{2.5}Li_{0.5}]Si_4O_{10}F_2$ as a function of frequency and temperature. While the bulk region ($\varepsilon'_b(0) = 10$) is hardly seen in this representation, the g.b. response ($\varepsilon'_{gb}(0) = 360$) and electrode polarization ($\varepsilon'_p(0)>10^6$) dominate the isotherms, which were recorded from 133 to 433 K in steps of 20 K. (b) Temperature behavior of the electric resistivity is expressed as M''/ω and measured at two different frequencies $\omega/2\pi = 1.2$ and 10.0 MHz. The fact that the flanks at high temperatures do not coincide is an indication of low-dimensional ion transport; 3D ion dynamics would yield the behavior indicated by the dashed-dotted lines. From the peak maxima, two electrical relaxation rates can be deduced that are also included in Figure 3b. See text for further explanations.

corresponds to an electrical process that is dominated by g.b. regions.[75] Increasing the frequency further leads to the associated dispersive part (C) of the DC plateau, which follows a $\sigma' \propto \nu^{p=1}$ behavior as indicated by the dashed line in Figure 3a.

With decreasing temperature, $\sigma'_{DC,\,gb}$ decreases and the curves are shifted toward lower frequencies. At sufficiently low T, a second DC plateau could be revealed (see regime II). This plateau does only appear as a curvature of the isotherms shown in regime II of Figure 3a. Its dispersive regime is only hardly visible; at very low temperatures and high frequency, the exponent p in the Jonscher-type relation $\sigma' \propto \nu^p$ approaches 1, indicating the beginning of a nearly constant loss behavior.[76−81] Most importantly, while total conductivities, domi-

https://dx.doi.org/10.1021/acs.chemmater.0c02460
Chem. Mater. 2020, 32, 7445−7457

nated by the g.b. response, can easily be read off from the distinct plateaus in regime I (see Figure 3a), $\sigma'_{DC,\,b}$ values characterizing bulk ion transport are only accessible by careful evaluation of the curvature seen in regime II. Filled symbols in Figure 3a mark estimations of these values.

The temperature dependence of both values, $\sigma'_{DC,\,b}$ and $\sigma'_{DC,\,gb}$, is analyzed using the Arrhenius plot shown in Figure 3b. Conductivities dominated by ion-blocking grain boundaries obey the Arrhenius law with an activation energy $E_{a\,gb}$ of 0.58 eV. Lines in Figure 3b refer to $\sigma'_{DC}T = \sigma_0$ exp. $(-E_a/(k_BT))$ with σ_0 being the pre-exponential factor and k_B denoting Boltzmann's constant. Compared to $\sigma'_{DC,\,gb}$ the bulk conductivity values $\sigma'_{DC,\,b}$ turned out to be higher by 6 orders of magnitude, and bulk ion transport has to be characterized by an activation energy of $E_{a,\,b}$ = 0.36 eV. Extrapolating the estimated values $\sigma'_{DC,\,b}$ toward room temperature yields 0.14 mS cm^{-1} at 293 K. This value is comparable to those reported for garnet-type oxides such as cubic-$Li_7La_3Zr_2O_{12}$ being considered as powerful electrolytes for ceramic electrochemical energy storage systems.[10]

To support our claim that the curvatures in regime II of Figure 3a are suitable to estimate bulk ion conductivities of hectorite-type $Li_{0.5}[Mg_{2.5}Li_{0.5}]Si_4O_{10}F_2$, we analyzed electric modulus curves, $M''(\nu)$, which we recorded at a fixed temperature and variable frequencies.[48] The corresponding curves are shown in Figure 4a by using a half-logarithmic plot and in Figure 4b by taking advantage of the double-logarithmic scaling to illustrate the change of M'' with frequency.

In general, the complex modulus $\boldsymbol{M}^*$ is given by the inverse complex permittivity, $M^* = 1/\boldsymbol{\varepsilon}^*$. The real part of $\boldsymbol{\varepsilon}^*$, denoted as ε', is shown in Figure 5a. As seen for σ', also $\varepsilon'(\nu)$ passes through the same electrical regimes viz. electrode polarization, g.b., and bulk response. The latter is only slightly seen for the isotherms recorded at very low temperatures. The permittivity value $\varepsilon'_b(\nu \rightarrow 0) = 10$ (see Figure 5a) corresponds to $C_b < 10$ pF if we use the relation for a plate capacitor, $C = \varepsilon_0\varepsilon'_bA/d$, to estimate the associated bulk capacitance. Here, ε_0 is the vacuum permittivity, A denotes the area of the pellet and d its thickness. Importantly, the imaginary part of M^*, M'', is dominated by bulk effects as the amplitude of M'' is proportional to the inverse of $C_{b,\,(gb)}$, $M'' \propto 1/C$. Hence, we expect a clearly visible bulk $M''(\nu)$ peak accompanied by a second one, the g.b. response, being drastically reduced in magnitude. As compared to the main peak, the g.b. peak (denoted as peak 1 in the following, see Figure 4b) is expected to be shifted toward lower frequencies by at least 6 orders of magnitude, as $\sigma'_{DC,\,gb}/\sigma'_{DC,\,b} \approx 10$.[6] While in the semilog plot, see Figure 4a, only the main peak (peak 2) is seen, in the double-logarithmic representation of the data, two modulus peaks are indeed recognizable, see the arrows in Figure 4b that exemplarily point to these two peaks that belong to the curve measured at 233 K. The ratio of the peak amplitudes is given by M''_{max}(peak 2)/M''_{max}(peak 1), which, in the present case, amounts to 30−40. Of course, this value reflects the ratio $\varepsilon'_{gb}/\varepsilon'_b$ (see Figure 5a) and the ratio C_{gb}/C_b as well. Note that these values are rough estimations, as they assume Debye-like responses. In general, deviations from Debye-like behavior are seen if correlated motion or, as argued in the following, low-dimensional transport governs the electrical relaxation processes.[82,83]

Here, the most important parameter, which we deduce from the two peaks of the modulus curves shown in Figure 4b, is the characteristic relaxation rate τ_M^{-1}. It corresponds to the frequency at which the peak appears, i.e., at $M'' = M''_{max}$. In Figure 3b, $\log_{10}(\tau_{M1}^{-1})$ and $\log_{10}(\tau_{M2}^{-1})$ of the two peaks 1 and 2 are plotted vs $1000/T$. $\tau_{M2}^{-1}(1/T)$ reveals almost the same activation energy (0.35 eV) as $\sigma'_{DC,\,b}$, thus supporting our interpretation of $\sigma'_{DC,\,b}$ to represent a parameter characterizing a bulk response. The difference in activation energies is less than 0.015 eV, which is within the error range of the values. The same holds for the activation energies obtained for τ_{M1}^{-1} and $\sigma'_{DC,\,gb}$ (0.60 eV vs 0.58 eV). Note that the rates τ_M^{-1} shown in Figure 3b refer to technical frequencies ν_{max}; using angular frequencies instead ($\omega_{max} = 2\pi\,\nu_{max}$) would simply shift the Arrhenius line by an additive constant ($\log_{10}(2\pi) \approx 0.8$) upward on the $\log_{10}$ scale.

In addition to the possibility to extract characteristic relaxation rates from $M''(\nu)$ peaks, we measured the quantity M''/ω as a function of the inverse temperature at a fixed frequency.[52,84,85] M''/ω corresponds to the resistivity ρ' and is expected to pass through an electrical relaxation peak that should be parameterizable with a Lorentzian shaped function: $\rho' = M''/\omega = \tau_\rho/(1 + (\tau_\rho\omega)^\beta)$ with $1<\beta\leq 2$. Here, τ_ρ denotes the electrical relaxation time, and β is a parameter that expresses the deviation of the peak, $\log_{10}(\rho')$ vs $1/T$, from symmetric behavior. Symmetric rate peaks are obtained for β = 2; $\beta<2$, however, indicates correlated motion affecting the electrical process probed. In the case of 3D motions, the latter case would result in asymmetric peaks with the so-called low-temperature flank, showing a lower slope than the high-temperature flank. If measured at different frequencies, the rates in the latter regime are expected to coincide. This feature is indicated in Figure 5b by the dashed-dotted lines. The activation energy of the high-T flanks should correspond to E_a sensed by $\sigma_{DC\,b}$ and τ_{M2}^{-1}, which are characterized by 0.36 eV. Astonishingly, in the present case, E_a in the high-T limit ranges from only 0.06 to 0.08 eV. Moreover, the high-temperature flanks of the two peaks clearly do not coincide. As an example, at 330 K, the corresponding values M''/ω differ by more than one order of magnitude revealing a dispersive behavior of the underlying electrical relaxation function. We attribute this deviation seen by the resistivity measurements to the low-dimension, i.e., 2D ionic transport in the Li-bearing phyllosilicate $Li_{0.5}[Mg_{2.5}Li_{0.5}]Si_4O_{10}F_2$. This assignment is considered to be in analogy to the interpretation of diffusion-induced NMR spin−lattice relaxation rate $(1/T_1)$ peaks as a function of the inverse temperature at various frequencies. In the case of, e.g., the 2D Li-ion conductor Li_xTiS_2, the dispersive behavior of the NMR correlation function in the high-T, that is, the low-frequency, limit was in *quantitative* agreement with the NMR theory.[40] Although, in principle, NMR and conductivity relaxation are governed by different correlation functions,[83,86] the conclusion that the high-T flank is sensitive to the dimensionality of diffusion holds *qualitatively* also for the resistivity.

At the peak maximum, i.e., at $T = T_{max}$, the condition $\tau_\rho\omega \approx 1$ is valid. With $\nu = \omega/2\pi$ for each frequency (ν = 1.2 MHz and ν = 10.0 MHz), a rate $\tau_\rho^{-1}(1/T_{max})$ can be estimated, which we included in Figure 3b as well. τ_ρ^{-1} agrees with τ_{M2}^{-1}deduced from the $M''(\nu)$ peaks if we extrapolate the corresponding Arrhenius line toward higher temperatures. Hence, long-range ion transport in the bulk of $Li_{0.5}[Mg_{2.5}Li_{0.5}]$-$Si_4O_{10}F_2$ is given by an activation energy of 0.35 eV. This value is comparable to those energies ordinarily seen for Li^+ ionic transport in, e.g., garnet-type oxides.[10,87,88] Identifying E_a = 0.35 eV with the activation energy, which should actually be

https://dx.doi.org/10.1021/acs.chemmater.0c02460
Chem. Mater. 2020, 32, 7445−7457

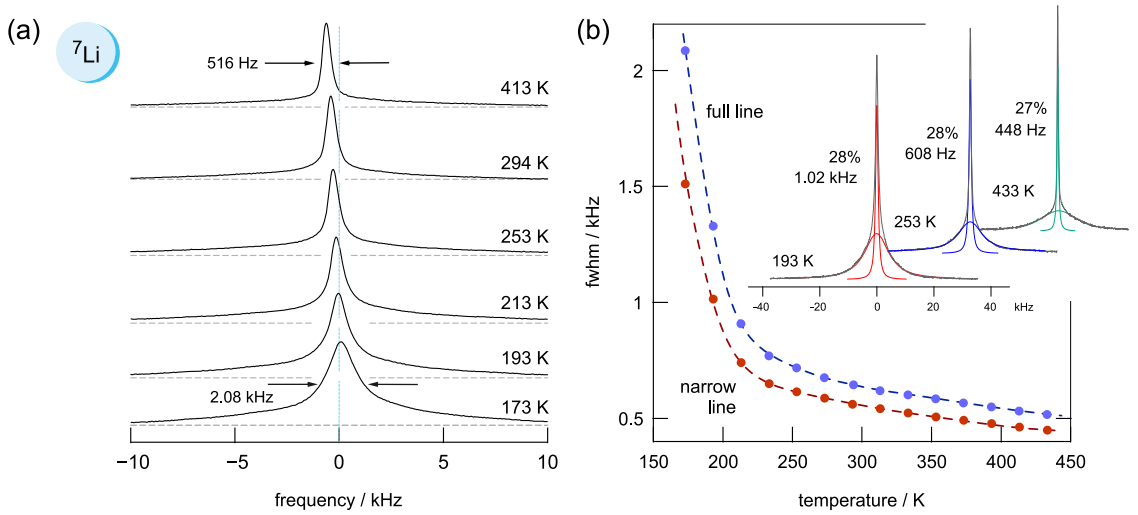

Figure 6. (a) ^{7}Li NMR line shapes recorded at the temperatures indicated. At 173 K, the fwhm of the superimposed complete line is given by 2.08 kHz. It reduces to 516 Hz at 413 K. This overall line is composed of two contributions; a deconvolution is seen in (b). In (b), the change of fwhm, either determined by using the full line shape or by analyzing the narrow component only, is shown as a function of temperature. Inset: deconvoluted ^{7}Li NMR spectra with the area of the Lorentzian (narrowed line) taking 28%, i.e., ca. 30%, of the full area under the line. See text for further explanation.

seen in the high-T regime of the $\rho'(1/T)$ peak, the parameter β would take a value of approximately 1.29, as β is given by 0.10 eV/0.35 eV = β − 1, if we adopt the analogy between conductivity and NMR relaxation more quantitatively.[5,30] In this relation, the value of 0.10 eV represents the activation energy in the low-T regime of the $\rho'(1/T)$ peak, see Figure 5b. β = 1.29 indicates rather strong ion−ion correlation effects. While such effects reduce the slope of the low-T flank, dimensionality effects will only influence the rates in the high-T regime. Semi-empirical models for 2D diffusion predict that the slope of the high-T flank should take a value that is approximately 75% of the slope in the low-T limit.[62] Here, the combination of ion−ion correlation and 2D diffusion results in apparently symmetric peak shapes even for low-dimensional dynamics. A very similar behavior has been observed earlier by Li^+ nuclear spin-relaxation in Li_xTiS_2.[40]

In conclusion, we found evidence that a 2D ionic transport is present in the phyllosilicate under study, which is governed by a rather low activation energy of only 0.35 eV. From Figure 3b, we see that the ratios $\tau_{M2}^{-1}/\tau_{M1}^{-1}$ (= τ_{M1}/τ_{M2}) and $\sigma'_{DC,\,b}/\sigma'_{DC,\,gb}$ differ by at least one order of magnitude. This observation is independent of T, as the differences in E_a for the two processes show only little change with temperature. Hence, we might have underestimated rather than overestimated the bulk ion conductivity, which we read off from the $\sigma'(\nu)$ curvatures seen in regime I (Figure 3a) by one order of magnitude. Such a rapid ionic transport process is expected to be measurable also in ^{7}Li nuclear spin relaxation. Indeed, both NMR line-shape measurements and spin-lock NMR spin−lattice relaxation rates point to temporary spin fluctuations being extremely rapid on the NMR time scale.

In Figure 6, ^{7}Li NMR line shapes are shown, which we recorded at temperatures ranging from 173 to 433 K. As can be seen in Figure 6b, the line consists of two components. A broader line with a width of ca. 12 kHz is superimposed by a narrower one whose width narrows with temperature because of increasing dipole−dipole averaging. Such averaging originates from motional processes rendering the homonuclear Li−Li dipolar interactions time dependent. The broad line can either be interpreted as a result of electric quadrupole interactions of the Li spins with nonvanishing electric field gradients or as a signal representing a group of Li ions with much lower diffusivity. As we do not recognize the emergence of a sharp quadrupole powder pattern at high temperatures, which would be in line with the universal temperature behavior of ^{7}Li NMR line shapes affected by averaging processes,[89,90] we assume that the broad line originates from a slow Li^+ subensemble. Most likely, this ensemble represents those ions sharing the same crystallographic position as Mg^{2+}. We assume that the Li ions located at 2*a*, i.e., between the layers, give rise to the narrow line observed.

To analyze the change in line width, we read off the fwhm of the total line; the line width as a function of temperature is shown in Figure 6. Starting from ca. 2 kHz, it reduces to values of ca. 500 Hz at 413 K, which is the so-called regime of extreme narrowing. We observe that the line width sharply increases at low temperature reaching 0.75 kHz at 250 K, at even higher temperatures, a shallower decrease is seen, which is still not fully completed at T = 450 K. To find out whether this is an exclusive feature of the overall line, we deconvoluted the lines with the help of a sum of a Lorentzian and a Gaussian function. Here, the narrow, Lorentzian-shaped line reveals the same temperature dependence as the overall line. The mainly homonuclear interactions of this line are averaged when T = 250 K is reached. Further averaging of residual couplings, likely between Li(2*a*) and Li(4 *h*), is seen at higher temperatures. Importantly, even at T = 173 K, the line has not reached its temperature-independent rigid-lattice value, i.e., rather rapid Li^+ exchange processes are present in $Li_{0.5}[Mg_{2.5}Li_{0.5}]Si_4O_{10}F_2$. We estimate that at 225 K, the associated average jump rate $1/\tau$ should be in the order of 10 kHz or higher, as full averaging will be achieved if $1/\tau$ greatly exceeds the spectral width of the NMR signal in the rigid lattice regime.

The deconvolution of the ^{7}Li NMR spectra tells us that approximately 30% (see the deconvoluted spectra shown in the inset of Figure 6b) of the total number of Li ions in $Li_{0.5}[Mg_{2.5}Li_{0.5}]Si_4O_{10}F_2$ have access to fast diffusion pathways, see the inset of Figure 6b. This value might be even higher, as

https://dx.doi.org/10.1021/acs.chemmater.0c02460
Chem. Mater. 2020, 32, 7445−7457

we cannot exclude that the broad component includes some quadrupole satellite intensities associated with the narrow line. In such a case, the value might reach 50%, which would be in line with what the chemical formula $Li_{0.5}[Mg_{2.5}Li_{0.5}]Si_4O_{10}F_2$ suggests. To shed light on this assumption, we recorded high-resolution ^{6}Li MAS NMR spectra, see Figure 7, for which first-order quadrupolar interactions and dipole−dipole broadening, both interactions being smaller for ^{6}Li anyway, are artificially averaged out through fast sample rotation. In agreement with the static line shapes, the ^{6}Li MAS line can be best approximated with a superposition of two distinct lines whereby the area under the narrow one again amounts to approximately 30%. A certain extent of Li−Mg exchange could serve as an explanation to understand the reduced spin density between the layers in $Li_{0.5}[Mg_{2.5}Li_{0.5}]Si_4O_{10}F_2$. For the sake of completeness, in Figure 7, the corresponding ^{19}F MAS NMR spectrum is shown, which reveals the two magnetically inequivalent F sites in $Li_{0.5}[Mg_{2.5}Li_{0.5}]Si_4O_{10}F_2$.

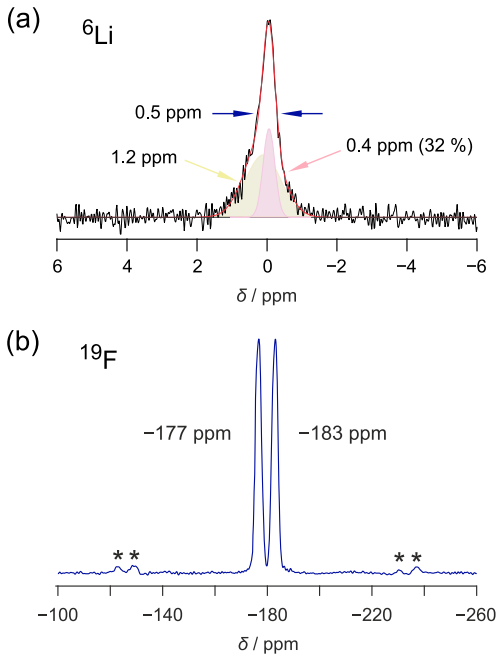

Figure 7. (a) ^{6}Li and ^{19}F MAS NMR spectra of $Li_{0.5}[Mg_{2.5}Li_{0.5}]Si_4O_{10}F_2$ recorded under ambient bearing gas conditions (300 K). The ^{6}Li MAS NMR spectrum can be best approximated with a combination of two spectral components as indicated. A deconvolution was possible with a sum of a Lorentzian line (narrow line) and a Gaussian one (broad line). Values denote line widths. Isotropic shifts were allowed to float. Approximately 32% of the Li ions, see also Figure 6b, are responsible for the narrow line. (b) In ^{19}F MAS NMR, two lines with equal intensities are seen reflecting the two magnetically inequivalent F sites in $Li_{0.5}[Mg_{2.5}Li_{0.5}]Si_4O_{10}F_2$. Asterisks mark spinning sidebands appearing at an interval of 25 kHz for each F signal.

The two-component features seen in both ^{7}Li and ^{6}Li NMR also affect the evolution of the magnetization transients, recorded in the former case, to extract diffusion-induced ^{7}Li NMR spin−lattice relaxation rates. As mentioned above, $M(t_d)$ can only be parameterized satisfactorily with a single, stretched exponential at sufficiently low temperatures (T<225 K). Above this threshold, which coincides with the beginning of the shallowly decaying part of the NMR line width (see Figure 6b), the transients start to follow a two-exponential time behavior, see also Figure S2. Therefore, we used a sum of two stretched exponentials, see the Supporting Information, to parameterize the overall transients; the same procedure, using the same terminology, is described in detail elsewhere.[31,70] The two rates $1/T_{1,slow}$ and $1/T_{1,fast}$ are shown in the Arrhenius plot of Figure 8a. The corresponding stretching exponents are displayed in the upper part of Figure 8. While $1/T_{1,slow}$ does not depend on temperature within the error limit of the analysis, $1/T_{1,fast}$ reveals a shallow diffusion-induced peak at T_{max} = 385 K. The low-T flank points to a very low activation energy of only 0.06 eV, which is likely to be dominated by strictly localized, i.e., short-range, Li^+ hopping processes and/or correlation effects.[30,32] Almost the same value was probed by the resistivity measurements, see Figure 5b.

Alternatively, we separated the two spectral contributions directly in the time domain of the underlying FIDs by individual analysis of the corresponding components that reveal quite different effective spin−spin relaxation rates. This procedure is described in detail elsewhere.[31,69,70,91] The FIDs are composed of a sharply (FID_{fast}) and a slowly decaying part (FID_{slow}), leading to two distinct rates, see Figure 7a. While the first decay reflects the broad spectral component, the latter decay, FID_{slow}, arises from the motionally narrowed component that represents fast Li^+ ions. At least for high temperatures, the rates associated with FID_{slow} agree with those obtained when analyzing the full $M(t_d)$ curves. Again, a relatively low activation energy of 0.12 eV can be estimated from the corresponding low-T flank. This value resembles that also seen in the resistivity peaks $\rho'(1/T)$ shown in Figure 5b, cf. the data recorded at 1.2 MHz. For the separated rates of the slow subensemble, a temperature independent behavior is seen for T>330 K.

To further characterize Li^+ ion hopping with methods that are also able to probe long-range ion dynamics, we performed variable-temperature spin-lock NMR measurements.[92] The corresponding $1/T_{1\rho}$ rates are shown in Figure 8b. The magnetization transients (Figure S2) do not allow for a separate investigation as it has been carried out for the $1/T_1$ measurements. Hence, they are to be regarded as averaged values. Likely, the fast Li^+ ions will dominate the overall nuclear spin response. Coming from low temperatures, the rates experience a sharp increase with temperature and pass through a maximum at T = 210 K; the maximum in$1/T_{1\rho}$ corresponds to a minimum in the stretching factor, see arrow in the upper graph of Figure 8b. The slope of the low-T flank of this prominent peak yields an activation energy of 0.39 eV, which is very similar to that seen by both conductivity spectroscopy and the modulus analysis, cf. the temperature dependence of $\sigma'_{DC,\,b}T$, and τ_{M2}^{-1} (Figure 3b). Thus, we found a strong indication that the peak probed by $1/T_{1\rho}$, which appeared at 205 K, reflects the same temporary fluctuations as detected by electrical relaxation. Interestingly, the activation energy of its high-T flank is comparable with those also characterizing the modulus peaks in Figure 5b. A value of 0.08 eV is also very similar to the estimated ones from $1/T_1$ NMR measurements (0.06 and 0.12 eV, see Figure 8a). Assuming a symmetric $1/T_1(1/T)$ peak, the activation energies in the high-T limit would be characterized by the same activation. In general, this similarity would be expected if the two methods probe the same (low-dimensional) diffusion process.[53] Importantly, dimensionality effects affect the slope of the NMR rate peaks in the high-T regime and yield apparent, reduced values.[32,43]

https://dx.doi.org/10.1021/acs.chemmater.0c02460
Chem. Mater. 2020, 32, 7445−7457

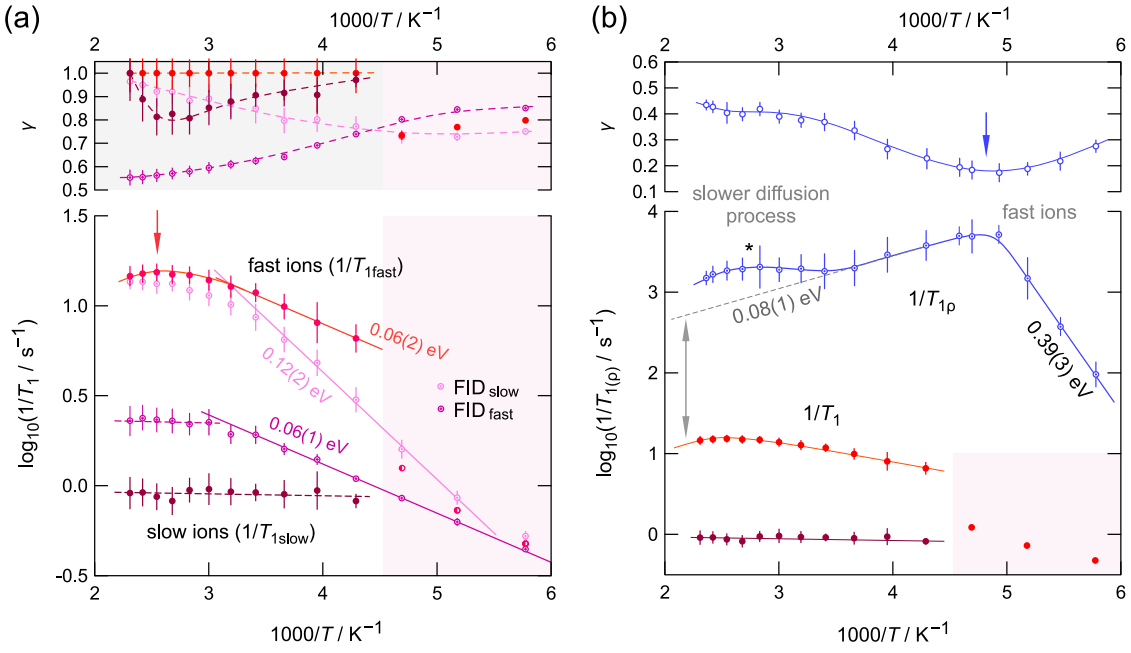

Figure 8. (a) ^{7}Li NMR spin–lattice relaxation rates of $Li_{0.5}[Mg_{2.5}Li_{0.5}]Si_4O_{10}F_2$ recorded in the laboratory frame of reference at a Larmor frequency of 116 MHz. The lower part shows an Arrhenius plot. The two-component ^{7}Li NMR line shape produces bi-exponential magnetization transients $M(t_d)$ leading to two rates $1/T_{1fast}$ and $1/T_{1slow}$ that reflect the fast and slow ions in Li-bearing fluorohectorite, also seen in ^{7}Li NMR lines. Alternatively, the stepwise analysis of the underlying FIDs also yields two relaxation rates. Stretching exponents γ are shown in the upper part of the figure. (b) Comparison of the spin-lock ^{7}Li NMR spin–lattice relaxation rates ($1/T_{1\rho}$, 20 kHz) with those measured in the laboratory frame of reference. The rate $1/T_{1\rho}$ passes through a diffusion-induced maximum at approximately 205 K. At this temperature, the corresponding γ passes through a minimum. Lines (dashed and solid) are to guide the eyes. Linear parts were analyzed with the Arrhenius law to extract the activation energies (in eV) as indicated.

In summary, electrical modulus measurements and spin-lock ^{7}Li NMR support the finding that long-range ion transport in hectorite-type $Li_{0.5}[Mg_{2.5}Li_{0.5}]Si_4O_{10}F_2$ is characterized by an activation energy of approximately 0.35 eV (see Figure 3b). In contrast to long-range transport, barriers with values of approximately 0.1 eV govern the local hopping processes. However, the values from high-T flanks, either seen in $1/T_{1\rho}$ or in $M''(\nu)$, are affected by dimensionality effects. As also recognized for the $M''(\nu)$ peaks, we observe that the rates $1/T_{1\rho}$ of the high-T flank do not coincide (see arrow in Figure 8b), with those expected from $1/T_1$ as is indicated by the dashed line in Figure 8b. This line extrapolates the high-T flank to even higher temperatures. The same feature is seen in Figure 5b. This dispersive behavior strongly supports our idea about 2D diffusion in the synthetic hectorite studied. Finally, $1/T_{1\rho}(1/T)$ revealed a second peak appearing at T_{max} = 350 K (marked by a star in Figure 8b), which, most likely, is to be assigned to the low translational ion mobility of the Li^+ ions sharing sites with Mg^{2+} in the layers of the phyllosilicate.

To directly compare the different responses seen by NMR and electrical relaxation, we finally estimated Li^+ jump rates from the maxima seen in $1/T_1$ and $1/T_{1\rho}$ at T_{max} = 385 K and T_{max} = 205 K, respectively, by using the maximum condition $\tau_{NMR}\omega_{0(1)} \approx 1$. The rates obtained are included in Figure 9. In the present case, they agree very well with those from electrical measurements. At 293 K, the Arrhenius line yields a mean jump rate $1/\tau$ of approximately 3×10^7 s^{-1}, which translates into a 2D diffusion coefficient $D_{2D} = a^2/(4\tau)$ of 4.7×10^{-13} m^2 s^{-1} if we use $a \approx 2.5$ Å. The crystallographic Li–Li distance is ca. 5 Å, which we think is too large for a single Li^+ jump. Assuming temporarily occupied interstitial positions connecting two or more regular sites in a distance of 2.5 Å seems to be more reasonable. $D = 4.7 \times 10^{-13}$ m^2 s^{-1} would indeed correspond to an estimated ionic conductivity σ_{est}, almost reaching the order of 0.1 mS cm^{-1} if we use the (idealized) cell

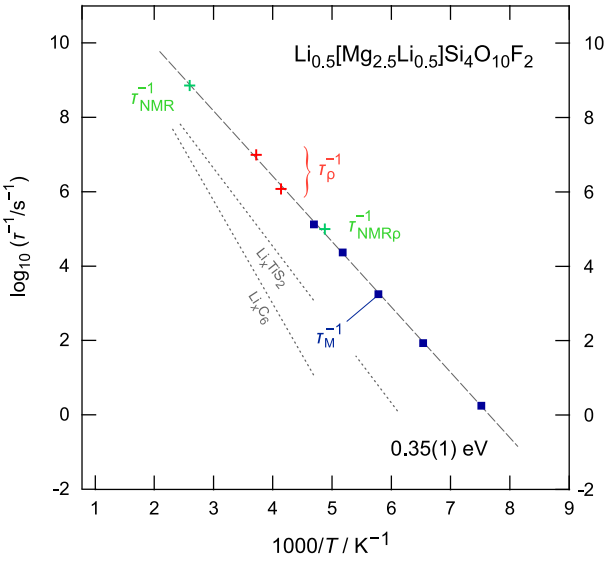

Figure 9. Arrhenius plot of the Li^+ hopping rates $1/\tau$ deduced from both nuclear spin relaxation and electrical relaxation taking advantage of the modulus representation and resistivity measurements, see Figure 3. Data from NMR, if restricted to the maxima of the spin–lattice relaxation rate peaks, agree well with the results from broadband electrical characterization. The dashed line represents a linear fit yielding 0.35(1) eV. For comparison, jump rates measured for Li_xTiS_2 (x = 0.7, 0.41 eV)[43] and Li_xC_6 (x = 1, 0.55 eV)[38] are also shown, see dotted lines.

https://dx.doi.org/10.1021/acs.chemmater.0c02460
Chem. Mater. 2020, 32, 7445–7457

volume of 490 Å^3 to estimate a charge carrier concentration of ca. $N^1 = 2 \times 10^{27}$ m^{-3}. $\sigma_{est.}$ is related to D_{NE} via the Nernst-Einstein relation, which reads in general $D_{NE} = \sigma k_B T/(N^1 q)$, with q being the charge of the Li^+ ions. We assumed that D_{2D} and D_{NE} are connected by $D_{2D} = (H_R/f)D_{NE}$ with H_R being the Haven ratio and f denoting the correlation factor. Our estimation anticipated H_R/f being of the order of unity. Taking into account that only 30% of the ions participate in Li^+ long-range ion transport, $D_{2D} = (H_R/f)D_{NE}$ is fulfilled if we chose $H_R/f \approx 0.3$. The relatively high value of D_{2D} obtained clearly renders hectorite as a fast ion conductor.

Rapid ion exchange in $Li_{0.5}[Mg_{2.5}Li_{0.5}]Si_4O_{10}F_2$ benefits from a wide interlayer gap giving the ions the necessary space to freely diffuse in the phyllosilicate. To the best of our knowledge, this is the first time that such high cation diffusivities were probed in a synthetic clay mineral. For comparison, in Figure 9, we included jump rates of two other 2D materials, Li_xTiS_2 (0.41 eV)[43] and LiC_6 (0.55 eV),[38] studied by NMR (and other methods) earlier. Inspired by the present results, one might think about crystal-chemical modifications that could lead to even higher diffusivities. Nature may offer a range of further silicate structures, including also layered ones, from which the necessary inspiration can be drawn to develop both powerful electrolytes and active materials for, e.g., lithium-ion batteries. Exemplarily, the Khan group studied hectorite-containing composite materials for this purpose.[56−59]

4. CONCLUSIONS

Li^+ ion diffusion and electrical transport in the hectorite-type phyllosilicate $Li_{0.5}[Mg_{2.5}Li_{0.5}]Si_4O_{10}F_2$ was studied by broad-band conductivity spectroscopy, modulus analysis, and ^{7}Li NMR spin−lattice relaxation measurements. Electrical and nuclear spin relaxation confirmed our hypothesis of rapid interlayer (2D) Li^+ exchange processes in the silicate. This process is characterized by an overall activation energy of approximately 0.35 eV. Under ambient conditions, conductivity spectroscopy points to an ionic conductivity as high as 0.14 mS cm^{-1}, representing a favorable starting point for further improvements by crystal-chemical engineering. In addition, we derived a consistent picture of Li^+ ion dynamics and showed that the electric and magnetic fluctuations probed originate from the same translational process. Our study supports the general idea that spatial confinement, able to guide the charge carriers over long distances, is helpful in enabling fast ion transport.

■ ASSOCIATED CONTENT

Supporting Information

The Supporting Information is available free of charge at https://pubs.acs.org/doi/10.1021/acs.chemmater.0c02460.

Simulated X-ray powder diffraction; ^{7}Li NMR magnetization transients from which the spin−lattice relaxation rates were extracted (PDF).

■ AUTHOR INFORMATION

Corresponding Authors

Paul Heitjans − *Institute of Physical Chemistry and Electrochemistry, Leibniz University Hannover, Hannover 30167, Germany;* orcid.org/0000-0003-1563-9176; Email: heitjans@pci.uni-hannover.de

H. Martin. R. Wilkening − *Institute for Chemistry and Technology of Materials, and Christian Doppler Laboratory for Lithium Batteries, Graz University of Technology, Graz 8010, Austria; Alistore−ERI European Research Institute, Amiens F-80039, France;* orcid.org/0000-0001-9706-4892; Email: wilkening@tugraz.at

Authors

Caroline Hiebl − *Institute for Chemistry and Technology of Materials, and Christian Doppler Laboratory for Lithium Batteries, Graz University of Technology, Graz 8010, Austria*

Patrick Loch − *Department of Chemistry and Bavarian Center for Battery Technology, University of Bayreuth, Bayreuth 95447, Germany*

Marina Brinek − *Institute for Chemistry and Technology of Materials, and Christian Doppler Laboratory for Lithium Batteries, Graz University of Technology, Graz 8010, Austria*

Maria Gombotz − *Institute for Chemistry and Technology of Materials, and Christian Doppler Laboratory for Lithium Batteries, Graz University of Technology, Graz 8010, Austria*

Bernhard Gadermaier − *Institute for Chemistry and Technology of Materials, and Christian Doppler Laboratory for Lithium Batteries, Graz University of Technology, Graz 8010, Austria;* orcid.org/0000-0003-2917-1818

Josef Breu − *Department of Chemistry and Bavarian Center for Battery Technology, University of Bayreuth, Bayreuth 95447, Germany;* orcid.org/0000-0002-2547-3950

Complete contact information is available at: https://pubs.acs.org/10.1021/acs.chemmater.0c02460

Author Contributions

#C.H. and M.B. contributed equally to this work.

Notes

The authors declare no competing financial interest.

■ ACKNOWLEDGMENTS

We thank the German Science Foundation (Deutsche Forschungsgemeinschaft (DFG)) for financial support (research unit FOR1277). Moreover, financial support from the Austrian Federal Ministry of Science, Research and Economy (BMWFW) and the National Foundation for Research, Technology and Development (CD-Laboratory of Lithium Batteries: Ageing Effects, Technology and New Materials) is gratefully acknowledged. The work also received funding from the European H2020 Framework program, no. 769929. P.H. is grateful to the State of Lower Saxony (Germany) for the Niedersachsen Professorship 'Mobility of Ions in Solids'.

■ REFERENCES

(1) Fergus, J. W. A review of electrolyte and electrode materials for high temperature electrochemical CO_2 and SO_2 gas sensors. *Sens. Actuators B Chem.* **2008**, *134*, 1034−1041.

(2) Fergus, J. W. Sensing mechanism of non-equilibrium solid-electrolyte-based chemical sensors. *J. Solid State Electrochem.* **2011**, *15*, 971−984.

(3) Rehman, A.; Zeng, X. Q. Ionic Liquids as Green Solvents and Electrolytes for Robust Chemical Sensor Development. *Acc. Chem. Res.* **2012**, *45*, 1667−1677.

(4) Gao, Z.; Sun, H.; Fu, L.; Ye, F.; Zhang, Y.; Luo, W.; Huang, Y. Promises, Challenges, and Recent Progress of Inorganic Solid-State Electrolytes for All-Solid-State Lithium Batteries. *Adv. Mater.* **2018**, *30*, 1705702.

(5) Uitz, M.; Epp, V.; Bottke, P.; Wilkening, M. Ion Dynamics in Solid Electrolytes for Lithium Batteries. *J. Electroceram.* **2017**, *38*, 142−156.
(6) Epp, V.; Wilkening, M. In *Handbook of Solid State Batteries*; Dudney, N. J.; West, W. C.; Nanda, J., Eds. World Scientific: Singapore, 2015; pp. 133−190.
(7) Lotsch, B. V.; Maier, J. Relevance of solid electrolytes for lithium-based batteries: A realistic view. *J. Electroceram.* **2017**, *38*, 128−141.
(8) Zhang, Z.; Shao, Y.; Lotsch, B.; Hu, Y.-S.; Li, H.; Janek, J.; Nazar, L. F.; Nan, C.-W.; Maier, J.; Armand, M.; Chen, L. New Horizons for Inorganic Solid State Ion Conductors. *Energy Environ. Sci.* **2018**, *11*, 1945−1976.
(9) Bachman, J. C.; Muy, S.; Grimaud, A.; Chang, H. H.; Pour, N.; Lux, S. F.; Paschos, O.; Maglia, F.; Lupart, S.; Lamp, P.; Giordano, L.; Shao-Horn, Y. Inorganic Solid-State Electrolytes for Lithium Batteries: Mechanisms and Properties Governing Ion Conduction. *Chem. Rev.* **2016**, *116*, 140−162.
(10) Thangadurai, V.; Narayanan, S.; Pinzaru, D. Garnet-type solid-state fast Li ion conductors for Li batteries: critical review. *Chem. Soc. Rev.* **2014**, *43*, 4714−4727.
(11) Chen, S.; Xie, D.; Liu, G.; Mwizerwa, J. P.; Zhang, Q.; Zhao, Y.; Xu, X.; Yao, X. Sulfide solid electrolytes for all-solid-state lithium batteries: structure, conductivity, stability and application. *Energy Storage Mater.* **2018**, *14*, 58−74.
(12) Janski, R.; Fugger, M.; Forster, M.; Sorger, M.; Dunst, A.; Hanzu, I.; Sternad, M.; Wilkening, M. Lithium barrier materials for on-chip Si-based microbatteries. *J. Mater. Sci. Mater. Electron.* **2017**, *28*, 14605−14614.
(13) Johnson, C. E.; Noda, K.; Roux, N. Ceramic breeder materials: Status and needs. *J. Nucl. Mater.* **1998**, *258-263*, 140−148.
(14) Roux, N.; Tanaka, S.; Johnson, C.; Verrall, R. Ceramic breeder material development. *Fusion Eng. Des.* **1998**, *41*, 31−38.
(15) Tang, T.; Zhang, Z.; Meng, J. B.; Luo, D. L. Synthesis and characterization of lithium silicate powders. *Fusion Eng. Des.* **2009**, *84*, 2124−2130.
(16) Quartarone, E.; Mustarelli, P. Electrolytes for solid-state lithium rechargeable batteries: recent advances and perspectives. *Chem. Soc. Rev.* **2011**, *40*, 2525−2540.
(17) Manthiram, A.; Yu, X.; Wang, S. Lithium battery chemistries enabled by solid-state electrolytes. *Nat. Rev. Mater.* **2017**, *2*, 16103.
(18) Zhang, B.; Tan, R.; Yang, L.; Zheng, J.; Zhang, K.; Mo, S.; Lin, Z.; Pan, F. Mechanisms and properties of ion-transport in inorganic solid electrolytes. *Energy Storage Mater.* **2018**, *10*, 139−159.
(19) Zheng, F.; Kotobuki, M.; Song, S.; Lai, M. O.; Lu, L. Review on solid electrolytes for all-solid-state lithium-ion batteries. *J. Power Sources* **2018**, *389*, 198−213.
(20) Ohno, S.; Bernges, T.; Buchheim, J.; Duchardt, M.; Hatz, A.-K.; Kraft, M. A.; Kwak, H.; Santhosha, A. L.; Liu, Z.; Minafra, N.; Tsuji, F.; Sakuda, A.; Schlem, R.; Xiong, S.; Zhang, Z.; Adelhelm, P.; Chen, H.; Hayashi, A.; Jung, Y. S.; Lotsch, B. V.; Roling, B.; Vargas-Barbosa, N. M.; Zeier, W. G. How Certain Are the Reported Ionic Conductivities of Thiophosphate-Based Solid Electrolytes? An Interlaboratory Study. *ACS Energy Lett.* **2020**, *5*, 910−915.
(21) Jay, E. E.; Rushton, M. J. D.; Chroneos, A.; Grimes, R. W.; Kilner, J. A. Genetics of superionic conductivity in lithium lanthanum titanates. *Phys. Chem. Chem. Phys.* **2015**, *17*, 178−183.
(22) Wang, Y.; Richards, W. D.; Ong, S. P.; Miara, L. J.; Kim, J. C.; Mo, Y.; Ceder, G. Design Principles for Solid-State Lithium Superionic Conductors. *Nat. Mater.* **2015**, *14*, 1026−1031.
(23) Richards, W. D.; Tsujimura, T.; Miara, L. J.; Wang, Y.; Kim, J. C.; Ong, S. P.; Uechi, I.; Suzuki, N.; Ceder, G. Design and Synthesis of the Superionic Conductor $Na_{10}SnP_2S_{12}$. *Nat. Commun.* **2016**, *7*, 1026−1031.
(24) He, X.; Zhu, Y.; Mo, Y. Origin of Fast Ion Diffusion in Superionic Conductors. *Nat. Commun.* **2017**, *8*, 15893.
(25) Di Stefano, D.; Miglio, A.; Robeyns, K.; Filinchuk, Y.; Lechartier, M.; Senyshyn, A.; Ishida, H.; Spannenberger, S.; Prutsch, D.; Lunghammer, S.; Rettenwander, D.; Wilkening, M.; Roling, B.; Kato, Y.; Hautier, G. Superionic Diffusion through Frustrated Energy Landscape. *Chem* **2019**, *5*, 2450−2460.
(26) Duvel, A.; Heitjans, P.; Fedorov, P.; Scholz, G.; Cibin, G.; Chadwick, A. V.; Pickup, D. M.; Ramos, S.; Sayle, L. W. L.; Sayle, E. K. L.; Sayle, T. X. T.; Sayle, D. C. Is Geometric Frustration-Induced Disorder a Recipe for High Ionic Conductivity? *J. Am. Chem. Soc.* **2017**, *139*, 5842−5848.
(27) Whittingham, M. S. Lithium Batteries and Cathode Materials. *Chem. Rev.* **2004**, *104*, 4271−4302.
(28) Whittingham, M. S. Inorganic Nanomaterials for Batteries. *Dalton Trans.* **2008**, 5424−5431.
(29) Epp, V.; Wilkening, M. Fast Li Diffusion in Crystalline $LiBH_4$ due to Reduced Dimensionality: Frequency-Dependent NMR Spectroscopy. *Phys. Rev. B* **2010**, *82*, 020301.
(30) Heitjans, P.; Schirmer, A.; Indris, S. NMR and β-NMR Studies of Diffusion in Interface-Dominated and Disordered Solids. In *Diffusion in Condensed Matter − Methods, Materials, Models*, Heitjans, P.; Kärger, J., Eds. Springer: Berlin, 2005; pp. 367−415.
(31) Heitjans, P.; Wilkening, M. Ion dynamics at interfaces: nuclear magnetic resonance studies. *Mater. Res. Bull.* **2009**, *34*, 915−922.
(32) Wilkening, M.; Heitjans, P. From Micro to Macro: Access to Long-Range Li^+ Diffusion Parameters in Solids via Microscopic ^6Li, ^7Li Spin-Alignment Echo NMR Spectroscopy. *Chem. Phys. Chem.* **2012**, *13*, 53−65.
(33) Kuhn, A.; Kunze, M.; Sreeraj, P.; Wiemhöfer, H. D.; Thangadurai, V.; Wilkening, M.; Heitjans, P. NMR Relaxometry as a Versatile Tool to Study Li Ion Dynamics in Potential Battery Materials. *Solid State Nucl. Magn. Reson.* **2012**, *42*, 2−8.
(34) McDowell, A. F.; Mendelsohn, C. F.; Conradi, M. S.; Bowman, R. C.; Maeland, A. J. 2-Dimensional Diffusion of Hydrogen in $ZrBe_2H_{1.4}$. *Phys. Rev. B* **1995**, *51*, 6336−6342.
(35) Vinod Chandran, C.; Heitjans, P. Solid-State NMR Studies of Lithium Ion Dynamics Across Materials Classes. *Annu. Rep. NMR Spectrosc.* **2016**, *89*, 1−102.
(36) Volgmann, K.; Epp, V.; Langer, J.; Stanje, B.; Heine, J.; Nakhal, S.; Lerch, M.; Wilkening, M.; Heitjans, P. Solid-State NMR to Study Translational Li Ion Dynamics in Solids with Low-Dimensional Diffusion Pathways. *Z. Phys. Chem. (NF)* **2017**, *231*, 1215−1241.
(37) Freiländer, P.; Heitjans, P.; Ackermann, H.; Bader, B.; Kiese, G.; Schirmer, A.; Stöckmann, H.-J.; Van der Marel, C.; Magerl, A.; Zabel, H. Diffusion-Processes in LiC_6 Studied by β-NMR. *Z. Phys. Chem. (NF)* **1987**, *151*, 93−101.
(38) Langer, J.; Epp, V.; Heitjans, P.; Mautner, F. A.; Wilkening, M. Lithium motion in the anode material LiC_6 as seen via time-domain ^7Li NMR. *Phys. Rev. B* **2013**, *88*, No. 094304.
(39) Winter, R.; Heitjans, P. Li^+ diffusion and its structural basis in the nanocrystalline and amorphous forms of two-dimensionally ion-conducting Li_xTiS_2. *J. Phys. Chem. B* **2001**, *105*, 6108−6115.
(40) Küchler, W.; Heitjans, P.; Payer, A.; Schöllhorn, R. ^7Li NMR relaxation by diffusion in hexagonal and cubic Li_xTiS_2. *Solid State Ionics* **1994**, *70-71*, 434−438.
(41) Wilkening, M.; Heitjans, P. Ultraslow diffusion in polycrystalline *h*-$LiTiS_2$ studied by ^7Li spin-alignment echo NMR spectroscopy. *Def. Diff. Forum* **2005**, *237-240*, 1182−1187.
(42) Wilkening, M.; Küchler, W.; Heitjans, P. From ultraslow to fast lithium diffusion in the 2D ion conductor $Li_{0.7}TiS_2$ probed directly by stimulated-echo NMR and nuclear magnetic relaxation. *Phys. Rev. Lett.* **2006**, *97*, 065901.
(43) Wilkening, M.; Heitjans, P. Li jump process in *h*-$Li_{0.7}TiS_2$ studied by two-time ^7Li spin-alignment echo NMR and comparison with results on two-dimensional diffusion from nuclear magnetic relaxation. *Phys. Rev. B* **2008**, *77*, No. 024311.
(44) Epp, V.; Nakhal, S.; Lerch, M.; Wilkening, M. Two-dimensional diffusion in $Li_{0.7}NbS_2$ as directly probed by frequency-dependent ^7Li NMR. *J. Phys. Condes. Matter.* **2013**, *25*, 195402.
(45) Stanje, B.; Epp, V.; Nakhal, S.; Lerch, M.; Wilkening, M. Li ion dynamics along the inner surfaces of layer-structured 2H-Li_xNbS_2. *ACS Appl. Mater. Interfaces* **2015**, *7*, 4089−4099.

https://dx.doi.org/10.1021/acs.chemmater.0c02460
Chem. Mater. 2020, 32, 7445−7457

(46) Langer, J.; Epp, V.; Sternad, M.; Wilkening, M. Diffusion-induced ^{7}Li NMR relaxation of layer-structured tin disulphide - Li diffusion along the buried interfaces in $Li_{0.17}SnS_2$. *Solid State Ionics* **2015**, *276*, 56−61.
(47) Epp, V.; Wilkening, M. Motion of Li^+ in nanoengineered $LiBH_4$ and $LiBH_4$:Al_2O_3 comparison with the microcrystalline form. *Chem. Phys. Chem.* **2013**, *14*, 3706−3713.
(48) Gombotz, M.; Lunghammer, S.; Breuer, S.; Hanzu, I.; Preishuber-Pflügl, F.; Wilkening, H. M. R. Spatial confinement - rapid 2D F^- diffusion in micro- and nanocrystalline $RbSn_2F_5$. *Phys. Chem. Chem. Phys.* **2019**, *21*, 1872−1883.
(49) Kuhn, A.; Sreeraj, P.; Pöttgen, R.; Wiemhöfer, H. D.; Wilkening, M.; Heitjans, P. Li Ion Diffusion in the Anode Material $Li_{12}Si_7$: Ultrafast Quasi-1D Diffusion and Two Distinct fast 3D Jump Processes Separately Revealed by ^{7}Li NMR Relaxometry. *J. Am. Chem. Soc.* **2011**, *133*, 11018−11021.
(50) Kuhn, A.; Dupke, S.; Kunze, M.; Puravankara, S.; Langer, T.; Pöttgen, R.; Winter, M.; Wiemhöfer, H. D.; Eckert, H.; Heitjans, P. Insight into the Li Ion Dynamics in $Li_{12}Si_7$: Combining Field Gradient Nuclear Magnetic Resonance, One- and Two-Dimensional Magic-Angle Spinning Nuclear Magnetic Resonance, and Nuclear Magnetic Resonance Relaxometry. *J. Phys. Chem. C* **2014**, *118*, 28350−28360.
(51) Nakhal, S.; Wiedemann, D.; Stanje, B.; Dolotko, O.; Wilkening, M.; Lerch, M. $LiBi_3S_5$ - A lithium bismuth sulfide with strong cation disorder. *J. Solid State Chem.* **2016**, *238*, 60−67.
(52) Preishuber-Pflügl, F.; Bottke, P.; Pregartner, V.; Bitschnau, B.; Wilkening, M. Correlated fluorine diffusion and ionic conduction in the nanocrystalline F^- solid electrolyte $Ba_{0.6}La_{0.4}F_{2.4}$ - ^{19}F T_{1r} NMR relaxation vs. conductivity measurements. *Phys. Chem. Chem. Phys.* **2014**, *16*, 9580−9590.
(53) Kuhn, A.; Narayanan, S.; Spencer, L.; Goward, G.; Thangadurai, V.; Wilkening, M. Li Self-Diffusion in Garnet-Type $Li_7La_3Zr_2O_{12}$ as Probed Directly by Diffusion-Induced ^{7}Li Spin-Lattice Relaxation NMR Spectroscopy. *Phys. Rev. B* **2011**, *83*, No. 094302.
(54) Breu, J.; Seidl, W.; Stoll, A. J.; Lange, K. G.; Probst, T. U. Charge homogeneity in synthetic fluorohectorite. *Chem. Mater.* **2001**, *13*, 4213−4220.
(55) Anthony, J. W., *Handbook of Mineralogy*. Mineral Data Pub.: Tucson, Ariz., 1990.
(56) Riley, M.; Fedkiw, P. S.; Khan, S. A. Transport Properties of Lithium Hectorite-Based Composite Electrolytes. *J. Electrochem. Soc.* **2002**, *149*, A667.
(57) Riley, M. W.; Fedkiw, P. S.; Khan, S. A. Lithium Hectorite Clay as the Ionic Conductor in $LiCoO_2$ Cathodes. *J. Electrochem. Soc.* **2003**, *150*, A933.
(58) Walls, H. J.; Riley, M. W.; Singhal, R. R.; Spontak, R. J.; Fedkiw, P. S.; Khan, S. A. Nanocomposite Electrolytes with Fumed Silica and Hectorite Clay Networks: Passive versus Active Fillers. *Adv. Funct. Mater.* **2003**, *13*, 710−717.
(59) Singhal, R. G.; Capracotta, M. D.; Martin, J. D.; Khan, S. A.; Fedkiw, P. S. Transport properties of hectorite based nanocomposite single ion conductors. *J. Power Sources* **2004**, *128*, 247−255.
(60) Yu, C.; Ganapathy, S.; de Klerk, N. J. J.; Roslon, I.; van Eck, E. R. H.; Kentgens, A. P. M.; Wagemaker, M. Unravelling Li-Ion Transport from Picoseconds to Seconds: Bulk versus Interfaces in an Argyrodite Li_6PS_5Cl-Li_2S All-Solid-State Li-Ion Battery. *J. Am. Chem. Soc.* **2016**, *138*, 11192−11201.
(61) Ganapathy, S.; Yu, C.; van Eck, E. R. H.; Wagemaker, M. Peeking across Grain Boundaries in a Solid-State Ionic Conductor. *ACS Energy Lett.* **2019**, *4*, 1092−1097.
(62) Richards, P. M., Magnetic Resonance in Superionic Conductors. In *Physics of Superionic Conductors*; Salamon, M. B., Ed., Topics in Current Physics, *Vol 15*, Springer: Berlin, 1979; pp. 141−(174) .
(63) Stöter, M.; Kunz, D. A.; Schmidt, M.; Hirsemann, D.; Kalo, H.; Putz, B.; Senker, J.; Breu, J. Nanoplatelets of Sodium Hectorite Showing Aspect Ratios of approximate to 20 000 and Superior Purity. *Langmuir* **2013**, *29*, 1280−1285.
(64) Rosenfeldt, S.; Stöter, M.; Schlenk, M.; Martin, T.; Albuquerque, R. Q.; Förster, S.; Breu, J. In-Depth Insights into the Key Steps of Delamination of Charged 2D Nanomaterials. *Langmuir* **2016**, *32*, 10582−10588.
(65) Daab, M.; Eichstaedt, N. J.; Edenharter, A.; Rosenfeldt, S.; Breu, J. Layer charge robust delamination of organo-clays. *RSC Adv.* **2018**, *8*, 28797−28803.
(66) Daab, M.; Eichstaedt, N. J.; Habel, C.; Rosenfeldt, S.; Kalo, H.; Schiebling, H.; Förster, S.; Breu, J. Onset of Osmotic Swelling in Highly Charged Clay Minerals. *Langmuir* **2018**, *34*, 8215−8222.
(67) Fukushima, E.; Roeder, S. B. W., *Experimental Pulse NMR. A Nuts and Bolts Approach*. Addison-Wesley Publ. Comp.: Reading, 1981.
(68) Look, D. C.; Lowe, I. J. Nuclear Magnetic Dipole-Dipole Relaxation along Static and Rotating Magnetic Fields - Application to Gypsum. *J. Chem. Phys.* **1966**, *44*, 2995−3000.
(69) Indris, S.; Heitjans, P. Heterogeneous ^{7}Li NMR Relaxation in Nanocrystalline Li_2O:B_2O_3 Composites. *J. Non-Cryst. Solids* **2002**, *307-310*, 555−564.
(70) Wilkening, M.; Indris, S.; Heitjans, P. Heterogeneous Lithium Diffusion in Nanocrystalline Li_2O:Al_2O_3 Composites. *Phys. Chem. Chem. Phys.* **2003**, *5*, 2225−2231.
(71) Kalo, H.; Müller, M. W.; Kunz, D. A.; Breu, J. How to maximize the aspect ratio of clay nanoplatelets. *Nanoscale* **2012**, *4*, 5633−5639.
(72) Gast, R. G.; Klobe, W. D. Sodium-Lithium Exchange Equilibria on Vermiculite at 25 Degrees and 50 Degrees C. *Clays Clay Miner.* **1971**, *19*, 311−319.
(73) Mermut, A. R.; Lagaly, G. Baseline studies of The Clay Minerals Society Source Clays: Layer-charge determination and characteristics of those minerals containing 2 : 1 layers. *Clays Clay Miner.* **2001**, *49*, 393−397.
(74) Kalo, H.; Milius, W.; Breu, J. Single crystal structure refinement of one- and two-layer hydrates of sodium fluorohectorite. *RSC Adv.* **2012**, *2*, 8452−8459.
(75) Irvine, J. T. S.; Sinclair, D. C.; West, A. R. Electroceramics: Characterization by Impedance Spectroscopy. *Adv. Mater.* **1990**, *2*, 132−138.
(76) Macdonald, J. R. Nearly Constant Loss or Constant Loss in Ionically Conducting Glasses: A Physically Realizable Approach. *J. Chem. Phys.* **2001**, *115*, 6192−6199.
(77) Funke, K.; Ross, I.; Banhatti, R. D. Nearly constant loss behavior in g-$RbAg_4I_5$: microwave conductivity plateau identified. *Solid State Ionics* **2004**, *175*, 819−822.
(78) Laughman, D. M.; Banhatti, R. D.; Funke, K. Nearly Constant Loss Effects in Borate Glasses. *Phys. Chem. Chem. Phys.* **2009**, *11*, 3158−3167.
(79) Laughman, D. M.; Banhatti, R. D.; Funke, K. New Nearly Constant Loss Feature Detected in Glass at Low Temperatures. *Phys. Chem. Chem. Phys.* **2010**, *12*, 14102−14108.
(80) Banhatti, R. D.; Laughman, D.; Badr, L.; Funke, K. Nearly Constant Loss Effect in Sodium Borate and Silver Meta-phosphate Glasses: New Insights. *Solid State Ionics* **2011**, *192*, 70−75.
(81) Rizos, A. K.; Alifragis, J.; Ngai, K. L.; Heitjans, P. Near constant loss in glassy and crystalline $LiAlSi_2O_6$ from conductivity relaxation measurements. *J. Chem. Phys.* **2001**, *114*, 931−934.
(82) Ngai, K. L., *Relaxation and Diffusion in Complex Systems*. Springer: New York, 2011, DOI: 10.1007/978-1-4419-7649-9.
(83) Habasaki, J.; León, C.; Ngai, K. L., *Dynamics of Glassy, Crystalline and Liquid Ionic Conductors*. Springer: New York, 2017; *132*.
(84) Munro, B.; Schrader, M.; Heitjans, P. AC Impedance Studies of Glassy and Crystalline Lithium Aluminosilicate Compounds. *Ber. Bunsenges. Phys. Chem. Chem. Phys.* **1992**, *96*, 1718−1723.
(85) Winter, R.; Siegmund, K.; Heitjans, P. Nuclear magnetic and conductivity relaxations by Li diffusion in glassy and crystalline $LiAlSi_4O_{10}$. *J. Non-Cryst. Solids* **1997**, *212*, 215−224.

(86) Bunde, A.; Dieterich, W.; Maass, P.; Meyer, M., Ionic Transport in Disordered Materials. In *Diffusion in Condensed Matter - Methods, Materials, Models*, Heitjans, P.; Kärger, J., Eds. Springer: Berlin, 2005; pp. 813−856.
(87) Buschmann, H.; Dölle, J.; Berendts, S.; Kuhn, A.; Bottke, P.; Wilkening, M.; Heitjans, P.; Senyshyn, A.; Ehrenberg, H.; Lotnyk, A.; Duppel, V.; Kienle, L.; Janek, J. Structure and Dynamics of the Fast Lithium Ion Conductor "$Li_7La_3Zr_2O_{12}$". *Phys. Chem. Chem. Phys.* **2011**, *13*, 19378−19392.
(88) Posch, P.; Lunghammer, S.; Berendts, S.; Ganschow, S.; Redhammer, G. J.; Wilkening, A.; Lerch, M.; Gadermaier, B.; Rettenwander, D.; Wilkening, H. M. R. Ion dynamics in Al-Stabilized $Li_7La_3Zr_2O_{12}$ single crystals - Macroscopic transport and the elementary steps of ion hopping. *Energy Storage Mater.* **2020**, *24*, 220−228.
(89) Bertermann, R.; Müller-Warmuth, W. Universality of NMR results in LISICON systems and other solid lithium conductors. *Z. Naturforsch. A J. Phys. Sci.* **1998**, *53*, 863−873.
(90) Bertermann, R.; Müller-Warmuth, W.; Jansen, C.; Hiltmann, F.; Krebs, B. NMR studies of the lithium dynamics in two thioborate superionic conductors: $Li_9B_{19}S_{33}$ and $Li_{4-2x}Sr_{2+x}B_{10}S_{19}$. *Solid State Ionics* **1999**, *117*, 245−255.
(91) Breuer, S.; Uitz, M.; Wilkening, H. M. R. Rapid Li Ion Dynamics in the Interfacial Regions of Nanocrystalline Solids. *J. Phys. Chem. Lett.* **2018**, *9*, 2093−2097.
(92) Epp, V.; Gün, Ö.; Deiseroth, H.-J.; Wilkening, M. Long-Range Li^+ Dynamics in the Lithium Argyrodite Li_7PSe_6 as Probed by Rotating-Frame Spin-Lattice Relaxation NMR. *Phys. Chem. Chem. Phys.* **2013**, *15*, 7123−7132.

https://dx.doi.org/10.1021/acs.chemmater.0c02460
Chem. Mater. 2020, 32, 7445−7457